Load Independent Constant Current and Constant Voltage Control of *LCC*-Series Compensated Wireless EV Charger

Veli Yenil and Sevilay Cetin

***Abstract*—In this article, load-independent constant current/voltage control operations of an *LCC*-Series compensated wireless electrical vehicle (EV) chargers are presented. The parameters of the *LCC*-Series compensation topology are designed based on load-independent zero phase angle and soft switching operation in the constant current charging operation. Then, the load independent soft switching conditions are achieved for constant voltage charging operation with a semibridgeless active rectifier using pulse density modulation control. Thus, high efficiency power transfer to the load is performed during the entire charging period. The wireless communication is not needed to achieve the output voltage regulation in the proposed EV charging system. The soft switching operations of the switches on the primary and the secondary side are achieved in a wide load range. The performance of the proposed charging system is validated by a prototype. At the full load condition, the output voltage of the system is regulated at 210 V while the output current is 5 A. The maximum efficiency is measured 93.8% at 1 kW output power with 150 mm air gap. The efficiency performance of the system is also evaluated based on the misalignment conditions.**

***Index Terms*—Constant current and constant voltage (CC/CV) charging, electrical vehicle, *LCC*-Series compensation, pulse density modulation, wireless power transfer.**

I. Introduction

NOWADAYS, wireless charging method is very popular for the charging application of the electrical vehicle (EV). Compared to contact charging method, no contact loss occurs, and no mechanical wear is required in wireless charging, it is safe and reliable [1], [2]. Another attractive feature of the wireless charging is that it provides dynamic charging allowing the battery charge while the vehicle is in the parking area or on the road [3]–[5].

The constant current/voltage charging operations are usually required during the charging process to provide the safety, durability and high performance of the battery [6], [7]. The basic charge profile including constant current (CC) and constant voltage (CV) operations is given in Fig. 1. In CC charging operation, the charge current is constant and load-independent while the charge voltage varies. The CV charge operation provides constant and load-independent charge voltage while the charge current varies [8], [9].

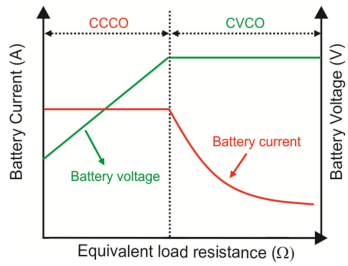

Fig. 1. Typical charging profile of the Li-ion battery.

The compensation network is usually used in the wireless charging system to compensate the reactive power caused by the large leakage inductance of loosely coupled coils [10], [11]. In the design of the compensation topologies, soft switching operation of the inverter switches and zero phase angle (ZPA) between the inverter output current and the voltage are taken into consideration [12]–[14]. The series–series (SS) topology is very popular in wireless chargers of EVs [15]–[17]. The SS compensation topology has the load-independent constant current characteristic at the resonance frequency [18]. However, the operation frequency needs to be changed to provide constant voltage output [19]. Low design freedom and high sensitivity to misalignment is another disadvantage of SS compensation topology [16].

In order to solve the shortcomings of SS compensation, high order compensation networks have been studied [20]–[23]. Among the many high order compensation network, double-sided *LCC* compensation topology has attracted more attention due to a lot of appealing features. However, more volume and weight are required on the receiver side since a double-sided *LCC* topology includes two resonant inductors and four resonant capacitors [24], [25].

The *LCC*-Series compensation, which provides high efficiency power transfer is another popular topology for EV charging applications [7], [14]. The power density of the *LCC*-Series topology is higher than double-sided *LCC* compensation since

Manuscript received June 29, 2021; revised September 29, 2021 and November 20, 2021; accepted January 15, 2022. Date of publication January 19, 2022; date of current version March 24, 2022. This work was supported by Pamukkale University under Grant 2020FEBE034. Recommended for publication by Associate Editor O. Onar. (*Corresponding author: Sevilay Cetin.*)

Veli Yenil is with the Department of Electrical and Electronics Engineering, Pamukkale University, 20160 Denizli, Turkey (e-mail: veliyenil@pau.edu.tr).

Sevilay Cetin is with the Department of Biomedical Engineering, Pamukkale University, 20160 Denizli, Turkey (e-mail: scetin@pau.edu.tr).

Color versions of one or more figures in this article are available at https://doi.org/10.1109/TPEL.2022.3144160.

Digital Object Identifier 10.1109/TPEL.2022.3144160

the *LCC*-Series topology has one resonant capacitor on the secondary side, which reduces size and weight. The *LCC*-Series topology has the load-independent CV output characteristic in essence [23]. A switching hybrid *LCC*-Series compensation topology is proposed in [7] to obtain the ZPA condition during the CC and CV charging period. However, additional switches and capacitors are required to maintain the ZPA condition during the entire charging period. In [26], a general unified design methodology is proposed to achieve load-independent CC and CV outputs at two different ZPA frequencies with an *LCC*-Series topology in accordance with the SAE J2954 [27]. However, the given method may lead to unpredictable self-inductance, mutual inductance, and power level of the coupling coils, so it cannot be effective in the use of practical applications. Because this method should simultaneously provide the change of self-inductance and the distance between the coupling coils, to ensure the charging requirements [28].

In [14], the output voltage and coupling variation are taken into consideration while the implementing the CC and CV charging operations of *LCC*-Series compensation. However, this method requires an additional dc–dc converter in the secondary side. The use of an additional dc–dc converter at the secondary side can be option to achieve CC or CV charging, as given in [29]–[31]. However, the use of additional converter increases the power conversion losses and the cost of the system.

In order to achieve CC and CV charging period of a WPT system, different control strategies have been proposed in the literature and can be categorized into three main types 1) primary side control; 2) secondary side control; 3) dual side control. In primary side control, frequency, phase, or duty control are usually applied to the primary side inverter [32]. However, the primary side control usually requires wireless communication, which is increasing the system complexity and the cost. In order to eliminate the wireless communication, Song *et al.* [33] proposed a primary side controller for CC and CV charging. However, additional hardware is required for the load resistance estimation and mutual inductance identification. In order to solve this, Li *et al.* [34] proposed a new primary side controller. However, an additional coil unit is needed to precise the control of CC charging, which increases size and reduces the power density of the WPT system.

In order to provide output regulation, an active rectifier can also be used in the secondary side [35]–[41]. The output regulation can be achieved by adjusting duty or phase of active rectifier. A dual side controlled inductive power transfer system is proposed according to the coupling coefficient variation and partial load condition in [35]. The proposed method eliminates the additional dc–dc converter. However, the wireless communication is needed to achieve the CC and CV output regulation. In addition, semi bridgeless active rectifier (S-BAR) switches operate with hard switching. In [36], the dual side phase shift (PS) control with impedance matching is implemented without using wireless communication. However, soft switching operation of both primary side inverter and S-BAR cannot be provided. So, the switching loss increases especially at light loads. A novel PS control for S-BAR is proposed in [37]. However, soft switching conditions cannot be achieved over a wide load range. In order to address this problem, frequency modulation controlled primary side inverter and PS-controlled S-BAR in [38] and variable frequency triple PS control in [39] are proposed. However, four variables are controlled to achieve the dual side soft switching under the large misalignment in [39]. In addition, detailed look up table is necessary to estimate mutual inductance. Recently, pulse density modulation (PDM) method is proposed to achieve dual side soft switching in [40] and [41]. In [40], PDM method with S-BAR at the secondary side of a WPT system is proposed. In [41], the PDM method is applied to dual side of the WPT system to realize not only voltage regulation but also efficiency maximization. However, PDM method commonly used in SS compensation and its optimization are difficult for high order topology. Generally speaking, many control methods of active rectifier as given in [35]–[41] use SS compensation, which strongly depends on the coupling coil parameters [16], [42].

When evaluated in terms of *LCC*-Series compensation topology, in [43], in order to realize ZVS operation in a wide power range, a variable frequency PS control method is presented for the systems with *LCC*-Series topology. The using the two modulation techniques together increases the control complexity. In addition, dynamic response of the system is affected due to multiple iterations. A hybrid control strategy of *LCC*-Series for wide output and ZVS range is presented in [44]. In the proposed method, the design procedure requires additional switch-controlled capacitor and communication between primary and secondary side. The self-tuning method for the parameter recognition of *LCC*-Series is presented in [45]. This method requires double side control and allows the system to operate in a large-scale coupling space. However, the output voltage of the proposed system depends on the mutual inductance. In addition, these studies are not focused on the entire CC and CV charging period.

According to the literature, limited studies have been proposed for the *LCC*-Series compensated WPT system providing CC and CV implementation with the use of S-BAR [46], [47]. However, none of them provide the dual side soft switching operation. The S-BAR has some advantages such as it can improve the power density and the efficiency of the secondary side. In [46], even if primary side inverter is operated with ZPA, the soft switching cannot be provided for S-BAR. In addition, it requires a complicated impedance tuning control based on turn on point and duty control of S-BAR resulting in hard switching. In [47], the PDM method with a distributed algorithm for the S-BAR in EV charging using *LCC*-Series compensation is proposed. However, this article includes only simulation results and experimental results were not given. Besides, simulation based PDM method is suggested only for CC mode, CV mode was not studied. In addition, the effects of PDM method on the inverter output current have not been investigated. It can be predicted that the effect of severe fluctuations of the input current of S-BAR on the inverter currents will be very noticeable, especially at light loads. The efficiency performance of the proposed article is also not presented.

In order to realize the dual side soft switching operation for a wide load range, a novel design approach based on PDM control for the load-independent CC and CV charging operations of the

LCC-Series WPT system using S-BAR is proposed in this article. The *LCC*-Series compensation topology is implemented according to the load-independent CC output design procedure. Then, S-BAR topology with PDM control is used at the secondary side to obtain load-independent CV output characteristic. According to this approach, the main contributions of this article can be listed as follows.

1) The entire charging period of the proposed WPT system using *LCC*-Series compensation is achieved at a constant operation frequency.
2) The load-independent CC and CV charging operations are provided without using additional component.
3) The soft switching operations are also provided for the inverter and the S-BAR switches.
4) The efficiency performance of entire charging period is improved, especially at light loads.
5) The output voltage regulation in CV charging operation is maintained at constant operation frequency under different misalignment conditions.
6) No communication is needed between primary and secondary side to regulate the output voltage.

First, the theoretical analysis of *LCC*-Series compensation topology based on load-independent CC output is presented. Then, hardware design including coupling coils, compensation topology, and PDM control strategy providing CV operation was defined. Finally, proposed design procedure was tested on a prototype. The output voltage is changed between 150 V and 210 V with 5 A in CC operation mode. In CV operation mode, the output voltage is regulated around 210 V while the output current is changed between 5 A and 1.25 A. The entire charging period of the proposed system is achieved at 85 kHz operation frequency. The maximum efficiency of the system is obtained in CC mode as 93.8% at 1 kW output power. The efficiency performance of the system was also compared to PS control, during CV charging operation. The soft switching operations of the inverter and the rectifier switches, the ZPA conditions were experimentally validated. The misalignment performance and transient response of the proposed system were separately tested in CC and CV charging operations. Finally, the performance of the proposed work was compared with similar works, recently proposed in the literature.

II. Theoretical Analysis

The proposed WPT system design using *LCC*-Series compensation consists of three parts: primary side inverter, resonant network, and S-BAR. The scheme of the proposed WPT system is shown in Fig. 2. V_{in} is the dc input voltage. S_1–S_4 are the switches of the primary side inverter. L_P and L_S are the primary and secondary self-inductances of the coupling coils, while M is the mutual inductance between two coils. L_{in}, C_p, and C_F are the primary side resonant elements, constituting of the *LCC* network. C_S is the secondary side resonant capacitor. The S-BAR topology consists of upper D_1–D_2 diodes and lower S_5–S_6 MOSFETs. i_{bat} is the output current, v_{bat} is the output voltage, R_{bat} represents the equivalent resistance of the battery, and C_o is the output filter capacitor.

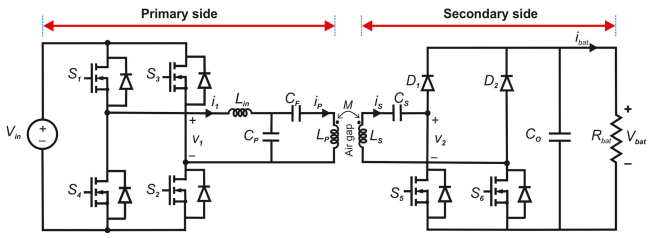

Fig. 2. Proposed WPT system.

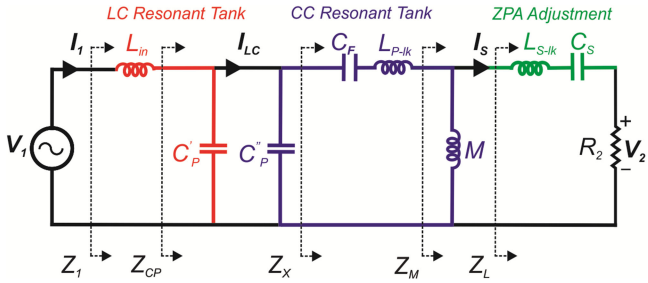

Fig. 3. T equivalent circuit model of *LCC*-Series topology for achieving ZPA in CC charging mode.

The fundamental harmonic analysis method is used to analyze the proposed WPT system. The M and T analytical models are widely used to analyze the coupling coils. The T equivalent circuit model of *LCC*-Series compensation topology for achieving ZPA in CC charging mode, according to given procedure in [7] and [22], is shown in Fig. 3. $\boldsymbol{V_1}$, $\boldsymbol{I_1}$ are the output voltage and the current of the primary side inverter. R_2 is the equivalent load resistor seen at the input of the S-BAR. $L_{P\text{-}lk}$ and $L_{S\text{-}lk}$ represent the primary and secondary side leakage inductance of the coupling coils, respectively. In Fig. 3, *LC* resonant tank is composed of L_{in} and $C_p{}'$. The $C_p{}''$, $L_{P\text{-}lk}$, C_F, and M represent the CC resonant tank. The output current of *LC* resonant tank is assumed constant for the CC output characteristic.

When the primary side inverter operates with 50% duty cycle, the relationship between the rms values of V_1 and V_{in} can be expressed as follows:

$$V_1 = \frac{2\sqrt{2}}{\pi} V_{in}. \tag{1}$$

For the S-BAR, the V_2 and I_S can be obtained by

$$V_2 = \frac{2\sqrt{2}}{\pi} V_{bat} \tag{2}$$

$$I_S = \frac{\pi}{2\sqrt{2}} I_{bat}. \tag{3}$$

The equivalent resistance of the S-BAR in the secondary side, R_2, can be calculated as

$$R_2 = \frac{8}{\pi^2} R_{bat}. \tag{4}$$

According to Fig. 3, $L_{P\text{-}lk}$ and $L_{S\text{-}lk}$ can be written as

$$L_{P-lk} = L_P - M \tag{5}$$

$$L_{S-lk} = L_S - M. \tag{6}$$

When L_{in} resonates with $C_p{}'$ at resonant frequency, the output current of the *LC* resonant circuit is sinusoidal and constant, which can be expressed as

$$\mathbf{I_{LC}} = -j\sqrt{\frac{C_P{}'}{L_{in}}} = -j\frac{V_1}{\omega_o L_{in}} \tag{7}$$

where ω_o is the angular resonant frequency of the system.

By applying Kirchhoff's current and voltage law, the current flowing through the secondary coil can be obtained as

$$\mathbf{I_S} = -j\frac{V_1 L_P{}'}{\omega_o M L_{in}} \tag{8}$$

where $L_p{}'$ can be defined as the equivalent inductance of the series connection of L_p and C_F since L_p is large enough.

C_P is equal to parallel combination of the $C_p{}'$ and $C_p{}''$, whose value given by

$$C_P = C_P{}' + C_P{}''. \tag{9}$$

The series connection of $L_{P\text{-}lk}$ and C_F is regarded as the equivalent inductance of L_x, whose value can be calculated as follows:

$$L_x = L_{P-lk} - \frac{1}{\omega_o^2 C_F}. \tag{10}$$

When $\mathrm{L_{in}}$ resonates with $C_p{}'$, $L_p{}'$ resonates with $C_p{}''$ and M resonates with $C_p{}''$ and L_x, the resonant conditions can be expressed as

$$\omega_o^2 = \frac{1}{L_{in}C_P{}'} = \frac{1}{L_P{}'C_P{}''} = \frac{1}{C_P{}''(L_x + M)}. \tag{11}$$

To reduce the volt-ampere rating and enhance the power transfer capability of the WPT system, the ZPA is necessary in the CC mode. According to Fig. 3, the secondary side load impedance Z_L can be calculated as

$$Z_L = j\omega_o L_{s-lk} + \frac{1}{j\omega_o C_S} + R_2. \tag{12}$$

The equivalent impedance of the secondary side referred to primary side Z_M can be calculated as

$$Z_M = j\omega_o M || Z_L = \frac{j\omega_o M Z_L}{j\omega_o M + Z_L}. \tag{13}$$

The equivalent impedance of Z_{CP} seen from C_P can be calculated as

$$Z_{CP} = \left[\left(j\omega_o L_{P-lk} + \frac{1}{j\omega_o C_F} + Z_M\right) || \frac{1}{j\omega_o C_P{}''}\right] || \frac{1}{j\omega_o C_P{}'}. \tag{14}$$

The input impedance of Z_1 can be calculated as follows:

$$Z_1 = Z_{Cp} + j\omega_o L_{in}. \tag{15}$$

According to (11), Z_1 can be simplified as

$$Z_1 = \frac{\omega_o^4 M^2 L_{in} C_P{}''}{\omega_o^2 L_P C_P{}' R_2 + j\omega_o^2 (X L_P C_P{}' - \omega_o M^2 C_P)}. \tag{16}$$

where X can be defined as

$$X = \omega_o L_{S-lk} - \frac{1}{\omega_o C_S}. \tag{17}$$

In order to provide the ZPA, imaginer component of $\mathrm{Z_1}$, given in (16), should be zero. Thus, ZPA condition can be controlled by using the following equation:

$$\omega_o M^2 C_P = X L_P C_P{}'. \tag{18}$$

Applying Kirchhoff's voltage and current laws to the equivalent circuit given in Fig. 3, the voltage gain, G_V, of the *LCC*-Series compensation network can be extracted as follows:

$$G_V = \frac{\mathbf{V_2}}{\mathbf{V_1}} = \frac{R_2 Z_M Z_{CP}}{Z_L Z_x Z_1}. \tag{19}$$

The output power consumed by R_2 can be expressed as

$$P_o = {I_{S-\mathrm{rms}}}^2 R_2. \tag{20}$$

The output power is rearranged by using (8), as follows:

$$P_o = \frac{V_{1-\mathrm{rms}}^2 {L_P{}'}^2}{\omega_o^2 M^2 {L_{in}}^2} R_2. \tag{21}$$

where $V_{1\text{-rms}}$ is the rms value $\boldsymbol{V_1}$.

III. Hardware Design

In this section, hardware design considerations for the design of *LCC*-Series compensation network, coupling coils, and constant voltage control strategy of the WPT system with 5 A output current in CC operation and 210 V output voltage in CV operation, respectively, are presented.

A. Coupling Coils Design

Coupling coils are play important role in a WPT system. In this article, a circular coil geometry is considered for both primary and secondary coils. The coupling coils are built with 18 turns ON both primary and secondary side. In the experimental prototype, litz wire is used to reduce the skin and proximity effects. Both the primary and the secondary coils are built with multiple litz wire (600 × 0.1 mm). The air gap between primary and secondary coils is about 15 cm. Both coils are consisted of N87 ferrite. The distribution of the magnetic flux density is calculated using three-dimensional finite element method (3-D FEM), which is performed in ANSYS Maxwell. For validating the simulation model, the coupling factor, primary and secondary inductances were measured under different lateral misalignment conditions at different air gaps. The measured and simulated self-inductances are shown in Fig. 4(a) and (b). The coupling coefficient variation is shown in Fig. 4(c) as a function of air gap under different lateral misalignment conditions. The design parameters of coupling coils are shown in Fig. 4(d) and the parameters are listed in Table I. The 3-D FEM simulation is time consuming process. So, the solve setup was configured with 7% percent error. Thus, the differences were occurred between the simulated and measured values. In addition, the coils were handmade in the experimental setup. Therefore, maintaining uniform turn spacing was not possible. Thus, a little difference in the outer dimension of the handmade coils was observed compared with 3-D FEM simulation. Nonetheless, the maximum error was obtained as 10 μH for the primary coil and 6.1 μH for the

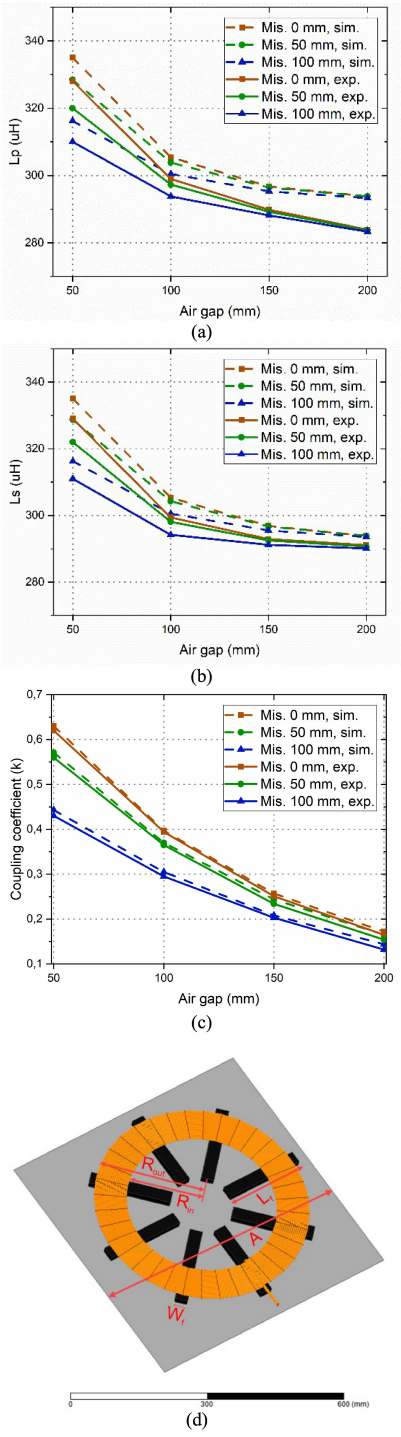

Fig. 4. Measurement and simulation results of coupling coils at different air gaps. (a) Primary self-inductance. (b) Secondary self-inductance. (c) Coupling coefficient. (d) Design parameters of coupling coils.

secondary coil. In Fig. 4(c), the maximum error was obtained 1.3% under 100 mm lateral misalignment at 50 mm air gap.

B. Design of LCC-Series Compensation Topology

The circuit parameters of the *LCC*-Series compensation topology are determined based on CC output characteristic, as given in Section II. The design procedure is presented in detail below.

TABLE I
DESIGN PARAMETERS OF COUPLING COILS

Symbol	Parameter	Value
L_P, L_S	Primary and secondary coil inductances	290 µH
R_{ac}	Ac resistance of primary and secondary coils	0.164 Ω
M	Mutual inductance	72.5 µH
k	Coupling coefficient	0.25
d	Air gap	150 mm
R_{in}	Inner radius of coupling coils	170 mm
R_{out}	Outer radius of coupling coils	245 mm
W_F	Width of ferrite bars	28 mm
L_F	Length of ferrite bars	186 mm
A	Outer diameter of circular pads	600 mm
	Ferrite bars	8

TABLE II
PARAMETERS OF THE *LCC*-SERIES COMPENSATION TOPOLOGY

Symbol	Parameter	Value
L_{in}	Resonant inductor	180 µH
C_P	Resonant capacitor	35.55 nF
C_S	Resonant capacitor	14.27 nF
C_F	Resonant capacitor	48.8 nF

First, the switching frequency is selected as 85 kHz, which is in compliance with SAE J2954 standard. In the next step, design specifications of the WPT system are determined, and the equivalent load resistance is calculated based on the specified constant output current and the voltage value of the battery. Then, primary compensation inductor $L_{\rm in}$ is determined as 180 μH. The obtained parameters of the *LCC*-Series compensation topology are shown in Table II.

The value of $C_p{}'$, $C_p{}''$, and C_P can be calculated as

$$C_P{}' = \frac{1}{\omega_o^2 L_{in}} \tag{22}$$

$$C_P{}'' = \frac{1}{\omega_o^2 (L_x + M)} \tag{23}$$

$$C_P = C_P{}' + C_P{}''. \tag{24}$$

The value of C_S, which satisfies the ZPA can be deduced from (16) as follows:

$$C_S = \frac{L_P{}' C_P{}'}{\omega_o^2 (L_P' L_S C_P{}' - M^2 C_P)}. \tag{25}$$

The value of C_F capacitor can be determined based on (10), as follows:

$$C_F = \frac{1}{(L_x - L_{P-lk})\omega_o^2}. \tag{26}$$

In order to verify the design method, the voltage and transconductance gain and the phase angle of the input impedance for *LCC*-Series compensation topology are given in Fig. 5. The ZPA is achieved at resonant frequency in CC charging. In addition, the output current in CC charging is constant at the resonant frequency of 85 kHz. Thus, the load independent CC

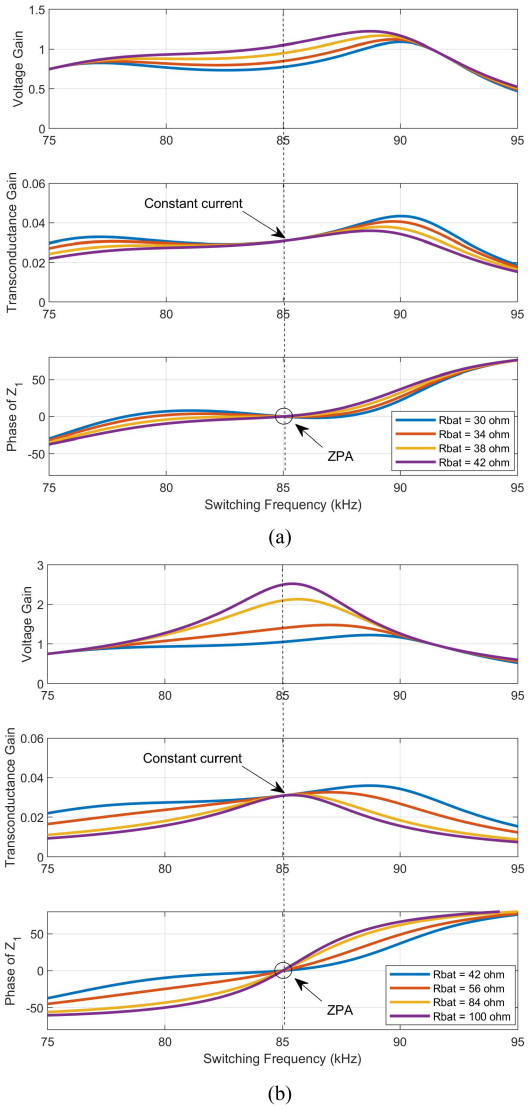

Fig. 5. Voltage, transconductance gain and phase angle of the input impedance of the *LCC*-Series compensation topology versus switching frequency. (a) CC output. (b) CV output.

charging with ZPA is achieved. When the WPT system operates in CV charging, the ZPA is also achieved at resonant frequency. However, as the load increases, the value of the output voltage increases. Therefore, the PDM method is applied to S-BAR switches to obtain constant output voltage in CV charging.

C. Constant Voltage Control Strategy

According to the analysis presented in previous section, the aim of the control strategy is to regulate the output voltage of the WPT system in CV charging control. For this purpose, S-BAR topology shown in Fig. 2 is used. Thus, no wireless communication between primary and secondary side is needed as the S-BAR topology controls the output voltage while the primary side inverter is operating at 85 kHz switching frequency with 50% duty ratio. In addition, it is possible to regulate the output voltage without changing any primary side control

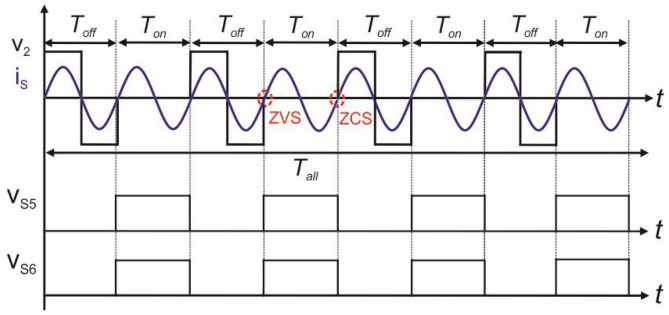

Fig. 6. Ideal waveforms of PDM control when pulse density value is 0.5.

parameters. Since the PDM control can achieve ZVS and ZCS for the switches of S-BAR, we preferred the PDM control in this work. The ideal waveforms of PDM control, when pulse density value is 0.5, is shown in Fig. 6. v_{S5} and v_{S6} represent the control signals of the S-BAR switches. In the PDM control, the output voltage V_{bat} and the output power are regulated by keeping the S_5–S_6 switches ON-state during the several resonant periods. The output is regulated with the controlling time $T_{\rm ON}$, of rectifier's switches within the determined time, $T_{\rm all}$, for PDM. S_5 and S_6 turn ON during $T_{\rm ON}$ while the traditional diode bridge turns ON during $T_{\rm OFF}$.

During the operation of S-BAR, S_5 and the antiparallel diode of S_6 are turned ON, in the positive half-cycle of v_2. In the negative half-cycle of v_2, S_6 and the antiparallel diode of S_5 are turned ON. Thus, the voltage across the input terminal of S-BAR is zero and no power is transferred to the load. The load is fed by the output filter capacitor. The S_5 and S_6 switches are turned ON at the zero crossing of the secondary coil current, i_S. Thus, ZVS turn-ON for S-BAR switches is achieved, as shown in Fig. 6.

The conventional diode bridge operates when the switches of the S-BAR are turned OFF. D_1 and antiparallel diode of S_6 transfer the power to the output, in the positive half-cycle of v_2. In the negative half-cycle of v_2, D_2 and the antiparallel diode of S_5 conduct the current and transfer the power to the output. As shown in Fig. 6, S_5 and S_6 are turned OFF at the zero crossing of i_S. Thus, diodes are naturally turned ON with ZCS, in the operation of the conventional diode bridge.

Based on the first harmonic approximation, the rms values of the input voltage and the input current of the S-BAR can be written, as follows:

$$V_{2-\rm rms} = \frac{2\sqrt{2}V_{bat}}{\pi}(1-d) \tag{27}$$

$$I_{S-\rm rms} = \frac{2\sqrt{2}V_{bat}}{\pi R_{bat}}(1-d) \tag{28}$$

where d represents the pulse density value. It can be given as

$$d = m \times \frac{T_{\rm on}}{T_{\rm all}} \tag{29}$$

where m represents the number of $T_{\rm ON}$ time determined in $T_{\rm all}$. The average power transferred to the load can be given

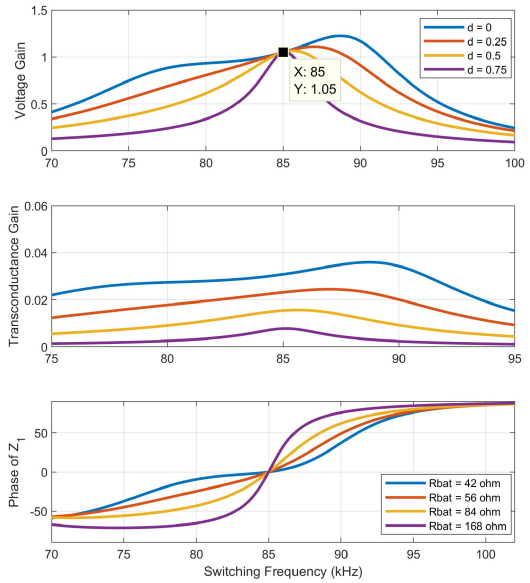

Fig. 7. Voltage and transconductance gain of the *LCC*-Series compensation topology versus switching frequency with PDM control.

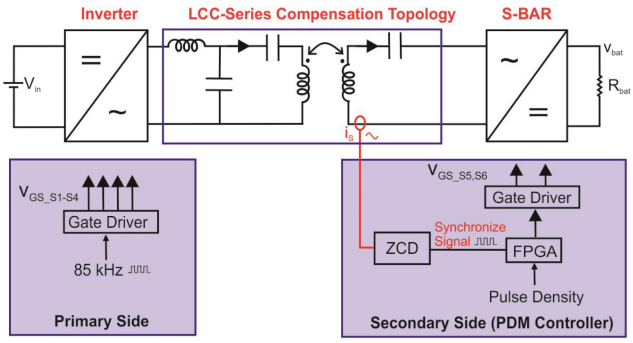

Fig. 8. Proposed WPT system with PDM control block diagram.

as follows:

$$P_{bat-\mathrm{PDM}} = \frac{8{V_{bat}}^2}{\pi^2 {R_{bat}}^2}(1-d)^2 R_2. \tag{30}$$

The maximum load power is obtained when d is equal to zero. With the PDM control strategy, the voltage and transconductance gain characteristics of the *LCC*-Series compensation topology are investigated. As shown in Fig. 7, the output voltage value is kept constant regardless of the load by changing the pulse density.

The proposed WPT system with PDM control is shown in Fig. 8. Primary side inverter is operated at 85 kHz switching frequency with 50% duty ratio. The control design is implemented in FPGA located on secondary side. The output voltage is controlled by adjusting d. The d is set in the FPGA to generate the control signals of the S_5–S_6 switches according to the PDM pattern of S-BAR. The driving signal of S_5–S_6 switches is synchronized with i_S. The zero-crossing points of i_s are captured by zero crossing detection (ZCD) circuit. Thus, ZVS and ZCS operations for the switches of S-BAR

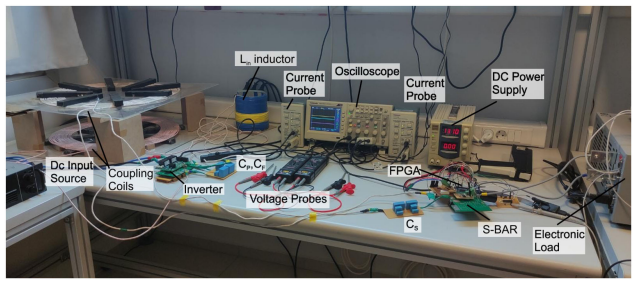

Fig. 9. Photograph of the prototype of the proposed WPT system.

are also provided. Therefore, the ZCD signal plays an important role in the PDM. Thanks to PDM, both the output current and the voltage regulation are provided at the constant switching frequency.

IV. Experimental Verification

A. Hardware Prototype

In order to verify the proposed design procedure, a laboratory prototype of the WPT system was built. The air gap between the coupling coils is to 150 mm. The *LCC*-Series resonant topology is configured based on the parameters listed in Table II. The input and the output voltages are 200 V and 210 V, respectively. The output current is constant at 5 A in CC operation. The measured values for the coupling coils were given in Table I. Both primary and secondary coils consisted of N87 ferrite material from EPCOS/TDK. High frequency polypropylene film capacitors are used for the design of compensation capacitors due to their low equivalent series resistance and high current carrying capability. Multiple capacitors are connected in series and parallel to achieve the theoretical value. The resonant inductor is constructed with litz wire to reduce the conduction losses. Since the voltage across of the compensation inductor is high due to the resonance, a helical air core coil with two layers is used. The primary side inverter was built with silicon carbide (SiC) MOSFETs (C2M0040120D from CREE). The S-BAR is built using 650 V SiC diode (C3D20065D from CREE) and 800 V power MOSFETs (IXFK34N80 from IXYS) at the secondary side. A Chroma dc Electronic Load was used to emulate the battery behavior. In the design of PDM controller, ZCD circuit for the secondary current is used. Thus, control pulses of S-BAR switches, produced in FPGA logic design, are applied at the correct time to achieve ZVS and ZCS operations. A high-speed analog comparator (LMV7219) and digital isolator (ADUM1100) were used in the implemented ZCD circuit. The secondary current was sensed by the use of a shunt resistor in the ZCD circuit. A photograph of the prototype of the proposed WPT system is given in Fig. 9.

B. Measured Waveforms and Efficiency Performance of CC/CV Charging Operations

First, CC charging operation is tested at two operation points. Fig. 10(a) and (b) shows experimental waveforms of v_1, i_1, v_{bat}, and i_{bat} in the CC charging mode. As shown in Fig. 10(a), the

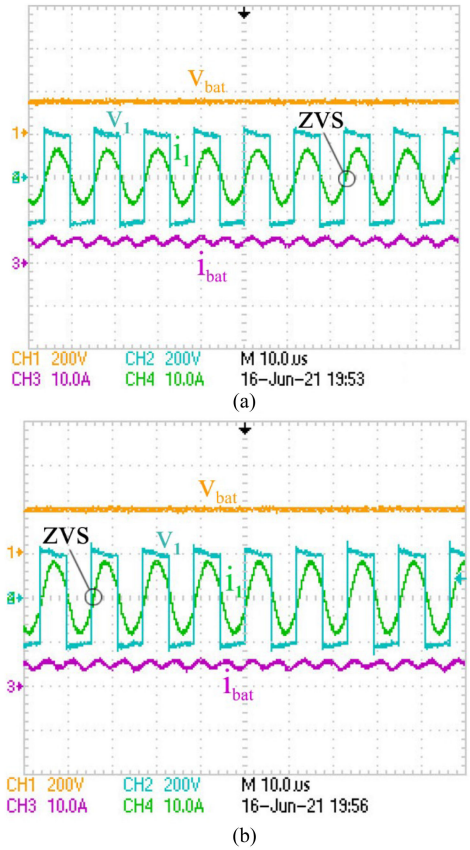

Fig. 10. Measured current waveforms of v_1, i_1, v_{bat}, and i_{bat} in the CC charging. (a) $V_{in} = 200$ V, $V_{bat} = 150$ V, and $i_{bat} = 5$ A. (b) $V_{in} = 200$ V, $V_{bat} = 210$ V, and $i_{bat} = 5$ A.

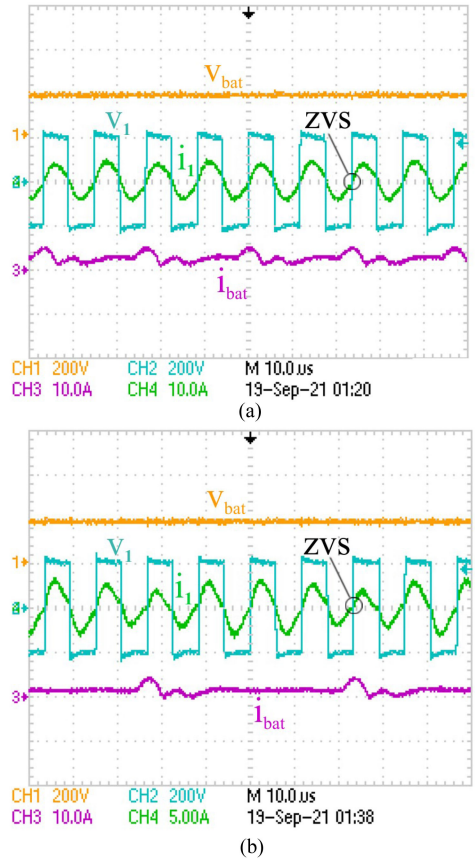

Fig. 11. Measured voltage and the current waveforms of v_1, i_1, v_{bat}, and i_{bat} in the CV charging. (a)$V_{in} = 200$ V, $V_{bat} = 210$ V, and $i_{bat} = 2.5$ A. (b) $V_{in} = 200$ V, $V_{bat} = 205$ V, and $i_{bat} = 1.25$ A.

output current i_{bat} is constant at 5 A, 750 W. Fig. 10(b) shows the output current i_{bat} is constant at 5 A, 1.05 kW. It can be observed in both figures that the ZVS condition for the inverter switches is achieved since the ZPA is achieved during the CC charging period.

Fig. 11(a) and (b) shows experimental waveforms of v_1, i_1, v_{bat}, and i_{bat} in the CV charging mode. The output voltage is obtained as 210 V at half load and 205 V at 25% load while the switching frequency is constant at 85 kHz. It is shown in both figures that soft switching operations are achieved during the CV charging period.

Fig. 12(a) and (b) shows experimental waveforms of v_1, i_1, $v_{2,}$ and i_S in the CV charging mode at 50% and 25% load power, respectively. According to the obtained results, ZVS operation for the S_5, S_6 switches and ZCS operation for D_1, D_2 diodes were achieved. In addition, soft switching operation of the inverter switches was also achieved since the WPT system operated at resonance frequency. In order to provide the output regulation, d was adjusted to 0.5 and 0.75 for 50% and 25% load conditions, respectively.

Fig. 13 shows the measured efficiency of the proposed WPT system from dc input of the inverter to the output of the S-BAR in both CC and CV charging period. The efficiency performance of PDM control was compared with PS control. According to obtained values, PDM control significantly improves the efficiency at light load conditions of CV charging operation. The efficiency in CC operation is same since the *LCC*-Series topology is designed with CC output characteristic at a constant operation frequency. The peak efficiency of the system is obtained as 93.8% at 1 kW in CC charging operation.

C. Output Voltage Regulation Performance

When the load is increased from 42 to 168 Ω, the PDM is enabled, and the pulse density is increased according to load variation. In order to provide sensitive output voltage regulation, especially light loads and under any misalignment condition, 256 resonant periods within the determined time T_{all}, for PDM, were implemented. Thus, the output voltage is kept constant around 210 V. The maximum output voltage fluctuation of the WPT is only 0.81% in CV charging. Fig. 14 shows the analytical and experimental values of the output voltage as a function of the load condition. When the load changes from full to 25%, the pulse density is changed between 0 and 1. As shown in the obtained values, analytical and experimental results are close each other and the difference between them can be acceptable.

D. Transient Response

In order to verify the CC and CV control, transient responses are given in Fig. 15. In CC charging operation, the output current

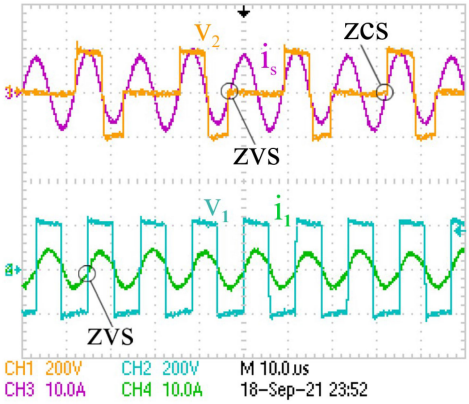

(a)

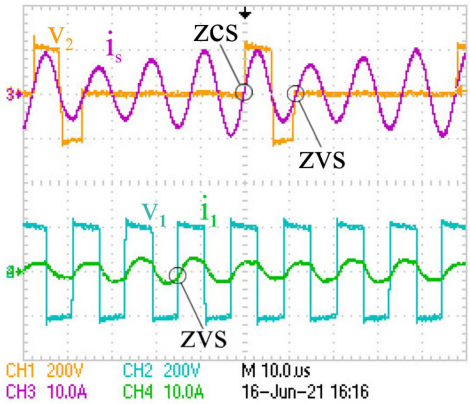

(b)

Fig. 12. Measured voltage and the current waveforms of v_1, i_1, v_2, and i_s in the CV charging mode. (a) 50% of full load power. (b) 25% of full load power.

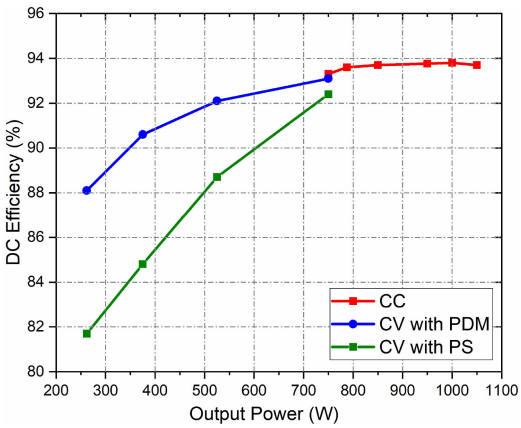

Fig. 13. Efficiency of the WPT system.

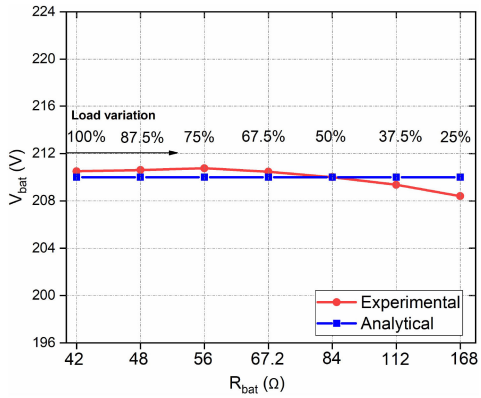

Fig. 14. Output voltage regulation of the WPT system with PDM.

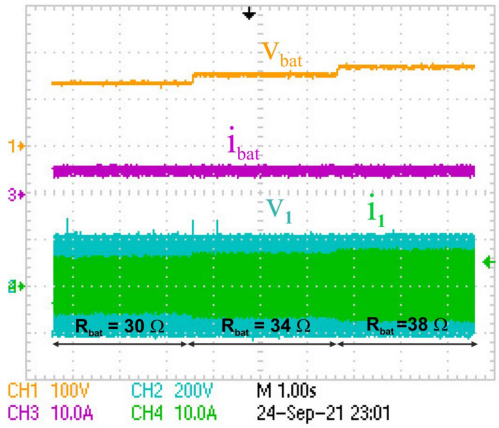

(a)

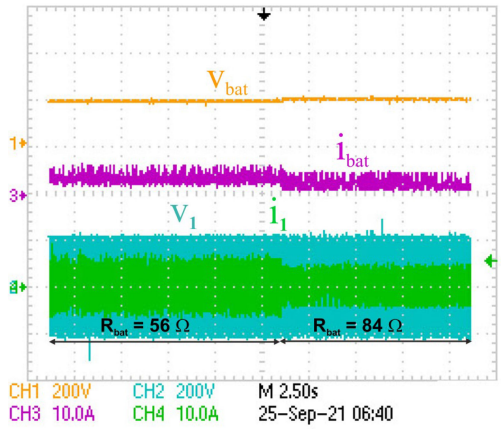

(b)

Fig. 15. Transient response of V_{bat}, i_{bat}, v_1, i_1 in (a) CC charging operation and (b) CV charging operation.

stays constant while the output voltage increases step by step. The output voltage rises from 150 to 190 V and the output current is constant 5 A, as shown in Fig. 15(a). In CV charging operation, when the load changes from 75% to 50%, the output voltage is nearly kept constant. As shown in Fig. 15(b), the output voltage was measured around 210 V, during the output current changes from 3.75 to 2.5 A.

E. Misalignment Performance

In practical applications, the misalignment between primary and secondary coils may occur. Due to misalignment of coupling coils, the coupling coefficient deviates from its nominal value, which affects the output current and voltage of the WPT system. Therefore, the performance of the WPT system should be considered when misalignment occurs. The output voltage regulation and the measured system efficiency under the different

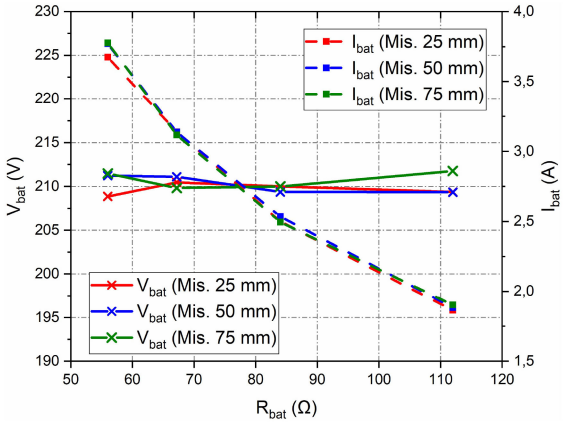

Fig. 16. Output voltage regulation of the WPT system under different misalignment and the load conditions, in CV charging operation.

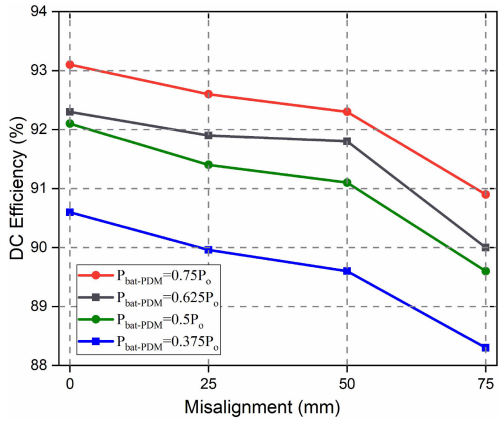

Fig. 17. Efficiency of the WPT system under different misalignment and the load conditions, in CV charging operation.

misalignment conditions are shown in Figs. 16 and 17, respectively. In the measurements, the WPT system is tested to have a lateral misalignment in the range of 0–75 mm, while the load changes between 0.363 and 0.787 kW, in CV charging. Based on the measurement results, the output voltage regulation is nearly kept around 210 V while the load and misalignment change. As well known, the efficiency of the WPT system decreases as the misalignment increases. As can be seen from Fig. 17; the efficiency values changes while the misalignment increases and the load decreases. In case of 75 mm lateral misalignment, the efficiency value of the WPT system is measured as 88.3% at 37.5% load conditions.

In order to test the misalignment performance of the proposed WPT system, in CC charging operation, lateral misalignment in the range of 0–75 mm is implemented. The measured efficiency values, as function of misalignment, obtained at constant 85 kHz operation frequency were given in Fig. 18. According to obtained values, when the misalignment changes between 0 and 75 mm, the output current changes between 5 and 5.55 A. In order to keep the output current constant at 5 A, under misalignment, the frequency control of primary side inverter is necessary. However, the frequency does not vary over a wide range to cope with misalignment. The CC output regulation of the system can be achieved between 85 and 92.17 kHz.

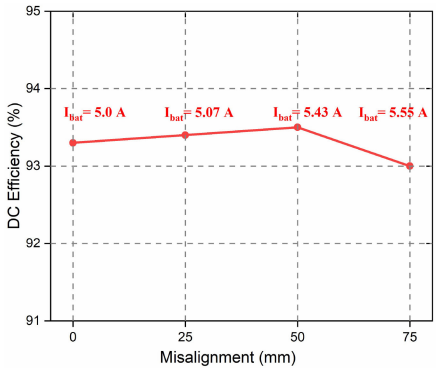

Fig. 18. Output current regulation of the WPT system under different misalignment conditions, in CC charging operation.

V. Comparison With the Other Methods

The PDM control method has been usually applied in SS topology. In SS topology, the output power of the proposed WPT system strongly depends on the parameters of coupling coils [7], [22], [16]. Thus, we decided to apply the PDM control to a high-order topology. In PDM control, some pulses are removed by controlling the switches on the primary side inverter or S-BAR. However, this is not an easy task for high-order topologies. The inverter current is seriously affected and the switching moments drift away from ZVS and ZCS due to duration time of PDM. Thus, this method losses its inherent advantages compared to the other control methods. So, PDM is not well suited for high order topologies as the primary side inverter causes unstable operation. However, the PDM control can be adapted to secondary side series high order topologies using S-BAR. With this control scheme, an improvement in the S-BAR efficiency is expected due to minimized switching losses compared to the other control methods. As a result, the proposed system can perform both CC and CV operation based on high efficiency power transfer with a single control method and single compensation topology in a very simple structure. Fig. 13 verifies the efficiency performance of the PDM control in CV charging operation, compared with the PS control.

In Table III, the proposed WPT system has been compared with the other studies, presented in the literature. The comparison parameters, including frequency, power transfer distance, efficiency, power rate, CC/CV charging performance, compensation topology, and misalignment, are given in Table III. When the studies are compared in terms of S-BAR control method, the switches of S-BAR in [35] and [37] are operated with hard switching due to PS control. Therefore, the overall efficiency in [35] is lower than our study. In [37], the efficiency performance is better than our study due to short air gap distance. However, when the efficiency results in [37] are compared in the same air gap, the efficiency performance of our study is better when the air gap distance is 15 cm. In the studies presented in [40] and [41], the PDM control was used for the secondary switches. However, CC charging and misalignment issue are not considered in both studies. In [38], frequency modulation controlled primary side inverter and PS-controlled S-BAR can realize soft switching. Misalignment issue is also discussed. Compared with [38], our

TABLE III
PERFORMANCE COMPARISON OF THE PROPOSED WPT SYSTEM

Frequency (kHz)	Power (kW)	Distance (mm)	Efficiency (%)	Compensation topology	CC/CV charging	Misalignment	Reference
35	3.3	170	92	SS	Both	Yes	[35]
150	1.0	80	94.4	SS	CV	Yes	[37]
30	7.5	40	74.2	SS	CV	No	[40]
917	0.05	500	70	SS	CV	No	[41]
50	0.151	N.A.	88.154	SS	Both	Yes	[38]
85	2.5	150	89.28	*LCC*-Series	Both	No	[7]
81.38–90	3.3	170	91.54	*LCC*-Series	Both	Yes	[46]
f_{CC}=90, f_{CV}=82	3.3	200	94.1	*LCC*-Series	Both	No	[26]
f_{CC} = 68, f_{CV} =79.1	6.6	200	96.1	Double-sided *LCC*	Both	No	[20]
85	1.05	150	93.8	*LCC*-Series	Both	Yes	Proposed work

WPT system performs better in terms of efficiency. In [7], hybrid *LCC*-Series compensation is proposed to achieve CC and CV charging under ZPA. However, the proposed system needs additional switches and passive components. Therefore, the overall system efficiency is low. In [20], the WPT system can achieve CC and CV charging under ZPA. However, misalignment issue is not considered in this article. In addition, the used compensation topology has a low power density. The method presented in [26] realizes the load independent CC and CV outputs at two different load independent ZPA frequencies, for the *LCC*-Series topology. However, the given method may lead to unpredictable self-inductance and mutual inductance of the coupling coils, so it cannot be effective in the use of practical applications [28]. Compared with [46], our system performs better in terms of efficiency thanks to soft switching operation of S-BAR. It can be concluded from Table III that the proposed WPT charger has competitive efficiency compared to the other WPT system thanks to PDM control of *LCC*-Series compensated WPT system including S-BAR circuit.

VI. CONCLUSION

In this article, the CC and CV performance of the WPT system with *LCC*-Series compensation topology is evaluated based on high efficiency power transfer. High efficiency is obtained by the use of S-BAR circuit topology at the secondary side. The proposed WPT system achieves the CC and CV charging at the constant operation frequency. The *LCC*-Series compensation topology is designed to be operated with ZPA as load-independent in CC operation. The PDM control adjusts the output voltage of the WPT system at 85 kHz as load independent in CV operation. Thus, entire charging period of the proposed system is provided at constant operation frequency as load-independent. In addition, the ZVS/ZCS conditions are achieved for the switches of S-BAR. Since the output voltage is controlled only in secondary side, a wireless communication between the primary and the secondary side is not needed during the output voltage regulation. To verify the performance of the WPT system, a prototype is built. The output voltage is regulated around 210 V in a wide load range. The peak efficiency of the WPT system is obtained as 93.8% in CC charging. The efficiency of CV charging operation was significantly improved. The output voltage regulation in CV charging control is varied around 0.81% while the load is changed from full to 25%. The PDM control also achieves the output voltage regulation, under different misalignment conditions.

REFERENCES

[1] D. Patil, M. K. McDonough, J. M. Miller, B. Fahimi, and P. T. Balsara, "Wireless power transfer for vehicular applications: Overview and challenges," *IEEE Trans. Transp. Electrific.*, vol. 4, no. 1, pp. 3–37, Mar. 2018.

[2] A. Ahmad, M. S. Alam, and R. Chabaan, "A comprehensive review of wireless charging technologies for electric vehicles," *IEEE Trans. Transp. Electrific.,* vol. 4, no. 1, pp. 38–63, Mar. 2018.

[3] J. Shin, S. Shin, Y. Kim, S. Ahn, and S. Lee, "Design and implementation of shaped magnetic resonance based wireless power transfer system for roadway-powered moving electric vehicles," *IEEE Trans. Ind. Electron.*, vol. 61, no. 3, pp. 1179–1192, Mar. 2014.

[4] R. Bosshard, U. Iruretagoyena, and J. W. Kolar, "Comprehensive evaluation of rectangular and double-D coil geometry for 50 kW/85 kHz IPT system," *IEEE J. Emerg. Sel. Topics Power Electron.*, vol. 4, no. 4, pp. 1406–1415, Dec. 2016.

[5] R. Bosshard and J. W. Kolar, "Multi-objective optimization of 50 kW/85 kHz IPT system for public transport," *IEEE J. Emerg. Sel. Topics Power Electron.,* vol. 4, no. 4, pp. 1370–1382, Dec. 2016.

[6] Z. Wang, X. Lai, and Q. Wu, "A PSR CC/CV flyback converter with accurate CC control and optimized CV regulation strategy," *IEEE Trans. Power Electron.*, vol. 32, no. 9, pp. 7045–7055, Sep. 2017.

[7] Y. Chen, H. Zhang, S. Park, and D. Kim, "A switching hybrid LCC-S compensation topology for constant current/voltage EV wireless charging," *IEEE Access,* vol. 7, pp. 133924–133935, Sep. 2019.

[8] G. Buja, M. Bertoluzzo, and K. N. Mude, "Design and experimentation of WPT charger for electric city-car," *IEEE Trans. Ind. Electron.*, vol. 62, no. 12, pp. 7436–7447, Dec. 2015.

[9] S. Dearborn, "Charging Li-ion batteries for maximum run times," *Power Electron. Technol. Mag.*, vol. 31, pp. 40–49, 2005.

[10] G. A. Covic and J. T. Boys, "Modern trends in inductive power transfer for transportation applications," *IEEE J. Emerg. Sel. Topics Power Electron.*, vol. 1, no. 1, pp. 28–41, Mar. 2013.

[11] W. Zhou and H. Ma, "Design considerations of compensation topologies in ICPT system," in *Proc. IEEE Conf. Appl. Power Electron.*, Mar. 2007, pp. 985–990.

[12] D. H. Tran, V. B. Vu, and W. Choi, "Design of a high-efficiency wireless power transfer system with intermediate coils for the on-board chargers of electric vehicles," *IEEE Trans. Power Electron.*, vol. 33, no. 1, pp. 175–187, Jan. 2018.

[13] S. Samanta and A. K. Rathore, "Analysis and design of load-independent ZPA operation for P/S, PS/S, P/SP, and PS/SP tank networks in IPT applications," *IEEE Trans. Power Electron.*, vol. 33, no. 8, pp. 6476–6482, Aug. 2018.

[14] M. Kim, D.-M. Joo, and B. K. Lee, "Design and control of inductive power transfer system for electric vehicles considering wide variation of output voltage and coupling coefficient," *IEEE Trans. Power Electron.*, vol. 34, no. 2, pp. 1197–1208, Feb. 2019.

[15] W. Zhang and C. C. Mi, "Compensation topologies of high-power wireless power transfer systems," *IEEE Trans. Veh. Technol.*, vol. 65, no. 6, pp. 4768–4778, Jun. 2016.
[16] W. Li, H. Zhao, J. Deng, S. Li, and C. C. Mi, "Comparison study on SS and double-sided LCC compensation topologies for EV/PHEV wireless chargers," *IEEE Trans. Veh. Technol.*, vol. 65, no. 6, pp. 4429–4439, Jun. 2016.
[17] J. L. Villa, J. Sallan, J. F. Sanz Osorio, and A. Llombart, "High misalignment tolerant compensation topology for ICPT systems," *IEEE Trans. Ind. Electron.*, vol. 59, no. 2, pp. 945–951, Feb. 2012.
[18] W. Zhang and C. C. Mi, "Compensation topologies of high-power wireless power transfer systems," *IEEE Trans. Veh. Technol.*, vol. 65, no. 6, pp. 4768–4778, Jun. 2016.
[19] W. Zhang, S. Wong, C. K. Tse, and Q. Chen, "Load-independent duality of current and voltage outputs of a series- or parallel-compensated inductive power transfer converter with optimized efficiency," *IEEE J. Emerg. Sel. Topics Power Electron.,* vol. 3, no. 1, pp. 137–146, Mar. 2015.
[20] V. B. Vu, D. H. Tran, and W. Choi, "Implementation of the constant current and constant voltage charge of inductive power transfer systems with the double-sided LCC compensation topology for electric vehicle battery charge applications," *IEEE Trans. Power Electron.,* vol. 33, no. 9, pp. 7398–7410, Sep. 2018.
[21] C. Liu, S. Ge, Y. Guo, H. Li, and G. Cai, "Double-LCL resonant compensation network for electric vehicles wireless power transfer: Experimental study and analysis," *IET Power Electron.,* vol. 9, no. 11, pp. 2262–2270, Sep. 2016.
[22] Y. Wang, Y. Yao, X. Liu, D. Xu, and L. Cai, "An LC/S compensation topology and coil design technique for wireless power transfer," *IEEE Trans. Power. Electron.*, vol. 33, no. 3, pp. 2007–2025, Mar. 2018.
[23] A. Ramezani, S. Farhangi, H. Iman-Eini, B. Farhangi, R. Rahimi, and G. R. Moradi, "Optimized LCC-series compensated resonant network for stationary wireless EV chargers," *IEEE Trans. Ind. Electron.,* vol. 66, no. 4, pp. 2756–2765, Apr. 2019.
[24] W. Li, H. Zhao, S. Li, J. Deng, T. Kan, and C. C. Mi, "Integrated LCC compensation topology for wireless charger in electric and plug-in electric vehicles," *IEEE Trans. Ind. Electron.,* vol. 62, no. 7, pp. 4215–4225, Jul. 2015.
[25] T. Kan, T.-D. Nguyen, J. C. White, R. K. Malhan, and C. C. Mi, "A new integration method for an electric vehicle wireless charging system using LCC compensation topology: Analysis and design," *IEEE Trans. Power Electron.,* vol. 32, no. 2, pp. 1638–1650, Feb. 2017.
[26] J. Lu, G. Zhu, D. Lin, Y. Zhang, J. Jiang, and C. C. Mi, "Unified load-independent ZPA analysis and design in CC and CV modes of higher order resonant circuits for WPT systems," *IEEE Trans. Transp. Electrific.,* vol. 5, no. 4, pp. 977–987, Dec. 2019.
[27] SAE international Standard, "J2954: Wireless charing of electric and plug-in hybrid vehicles," 2010. [Online]. Available: http://standards.sae.org/wip/j2954/
[28] L. Yang, X. Li, S. Liu, Z. Xu, and C. Cai, "Analysis and design of an LCCC/S compensated WPT system with constant output characteristics for battery charging applications," *IEEE J. Emerg. Sel. Topics Power Electron.,* vol. 9, no. 1, pp. 1169–1180, Feb. 2021.
[29] V. P. Galigekere, O. C. Onar, M. Chinthavali, and Z. J. Wang, "Load power agnostic 6.6 kW wireless EV charger with LCL tuned primary and secondary side regulation," *in Proc. IEEE Energy Convers. Congr. Expo.*, Cincinnati, OH, USA, Oct. 2017, pp. 4839–4844.
[30] Z. Li, C. Zhu, J. Jiang, K. Song, and G. Wei, "A 3-kW wireless power transfer system for sightseeing car supercapacitor charge," *IEEE Trans. Power Electron.,* vol. 32, no. 5, pp. 3301–3316, May 2017.
[31] Y. Yang, W. Zhong, S. Kiratipongvoot, S. Tan, and S. Y. R. Hui, "Dynamic improvement of series−series compensated wireless power transfer systems using discrete sliding mode control," *IEEE Trans. Power Electron.,* vol. 33, no. 7, pp. 6351–6360, Jul. 2018.
[32] J. M. Miller, O. C. Onar, and M. Chinthavali, "Primary-side power flow control of wireless power transfer for electric vehicle charging," *IEEE J. Emerg. Sel. Topics Power Electron.,* vol. 3, no. 1, pp. 147–162, Mar. 2015.
[33] K. Song, Z. Li, J. Jiang, and C. Zhu, "Constant current/voltage charging operation for series–series, and series-parallel compensated wireless power transfer systems employing primary-side controller," *IEEE Trans. Power Electron.,* vol. 33, no. 9, pp. 8065–8080, Sep. 2018.
[34] Z. Li, H. Liu, Y. Tian, and Y. Liu, "Constant current/voltage charging for primary-side controlled wireless charging system without using dual-side communication," *IEEE Trans. Power Electron*, vol. 36, no. 12, pp. 13562–13577, Dec. 2021.
[35] T. Diekhans and R. W. De Doncker, "A dual-side controlled inductive power transfer system optimized for large coupling factor variations and partial load," *IEEE Trans. Power Electron.,* vol. 30, no. 11, pp. 6320–6328, Nov. 2015.
[36] Z. Li, K. Song, J. Jiang, and C. Zhu, "Constant current charging and maximum efficiency tracking control scheme for supercapacitor wireless charging," *IEEE Trans. Power Electron.,* vol. 33, no. 10, pp. 9088–9100, Oct. 2018.
[37] K. Colak, E. Asa, M. Bojarski, D. Czarkowski, and O. C. Onar, "A novel phase-shift control of semibridgeless active rectifier for wireless power transfer," *IEEE Trans. Power Electron.,* vol. 30, no. 11, pp. 6288–6297, Nov. 2015.
[38] Z. Huang, S.-C. Wong, and C. K. Tse, "An inductive-power-transfer converter with high efficiency throughout battery-charging process," *IEEE Trans. Power Electron.,* vol. 34, no. 10, pp. 10245–10255, Oct. 2019.
[39] Y. Liu, U. K. Madawala, R. Mai, and Z. He, "An optimal multivariable control strategy for inductive power transfer systems to improve efficiency," *IEEE Trans. Power Electron.,* vol. 35, no. 9, pp. 8998–9010, Sep. 2020.
[40] M. Fan, L. Shi, Z. Yin, and Y. Li, "A novel pulse density modulation with semi-bridgeless active rectifier in inductive power transfer system for rail vehicle," *CES Trans. Elect. Mach. Syst.,* vol. 1, no. 3, pp. 397–404, Dec. 2017.
[41] H. Li, J. Fang, S. Chen, K. Wang, and Y. Tang, "Pulse density modulation for maximum efficiency point tracking of wireless power transfer systems," *IEEE Trans. Power Electron.,* vol. 33, no. 6, pp. 5492–5501, Jun. 2018.
[42] Y. Yao, Y. Wang, X. Liu, and D. Xu, "Analysis, design, and optimization of LC/S compensation topology with excellent load-independent voltage output for inductive power transfer," *IEEE Trans. Transp. Electrific.,* vol. 4, no. 3, pp. 767–777, Sep. 2018.
[43] H. Hu, T. Cai, S. Duan, X. Zhang, J. Niu, and H. Chen, "An optimal variable frequency phase shift control strategy for ZVS operation within wide power range in IPT systems," *IEEE Trans. Power Electron.*, vol. 35, no. 5, pp. 5517–5529, May 2020.
[44] X. Wang, J. Xu, M. Leng, H. Ma, and S. He, "A hybrid control strategy of LCC-S compensated WPT system for wide output voltage and ZVS range with minimized reactive current," *IEEE Trans. Ind. Electron.,* vol. 68, no. 9, pp. 7908–7920, Sep. 2021.
[45] W. Li, G. Wei, C. Cui, X. Zhang, and Q. Zhang, "A double-side self-tuning LCC/S system using a variable switched-capacitor based on parameter recognition," *IEEE Trans. Ind. Electron.*, vol. 68, no. 4, pp. 3069–3078, Apr. 2021.
[46] S. Ann and B. K. Lee, "Analysis of impedance tuning control and synchronous switching technique for a semi-bridgeless active rectifier in inductive power transfer systems for electric vehicles," *IEEE Trans. Power Electron.,* vol. 36, no. 8, pp. 8786–8798, Aug. 2021.
[47] J. H. Lee, W. -J. Son, S. Ann, J. Byun, and B. K. Lee, "Improved pulse density modulation with a distribution algorithm for semi-bridgeless rectifier of inductive power transfer system in electric vehicles," in *Proc. 10th Int. Conf. Power Electron. ECCE Asia*, 2019, pp. 1–6.

Veli Yenil was born in Denizli, Turkey. He received the B.S. and M.S. degrees in electrical and electronics engineering in 2014 and 2016, respectively, from Pamukkale University, Denizli, Turkey, where he is currently working toward the Ph.D. degree in electrical and electronics engineering.

His research interests include wireless power transfer and resonant converters.

Sevilay Cetin was born in Denizli, Turkey. She received the B.S. and M.S. degrees in electrical and electronics engineering from Pamukkale University, Denizli, Turkey, in 2001 and 2005, respectively, and the Ph.D. degree in electrical engineering from Yildiz Technical University, Istanbul, Turkey, in 2011.

From 2013 to 2014, she was a Postdoctoral Research Associate with NY State Center for Future Energy Systems, Rensselaer Polytechnic Institute, Troy, NY, USA. From 2012 to 2017, she was an Assistant Professor with the Department of Biomedical Engineering, Pamukkale University, Denizli, Turkey, where she is currently an Associate Professor. Her research interests include DC–DC, AC–AC converter topologies, soft-switching techniques, and high-efficiency and high power density power conversion for automotive, industrial, and biomedical applications.